

Physics-Driven Deep Learning for Computational Magnetic Resonance Imaging

Kerstin Hammernik, Thomas Küstner, Burhaneddin Yaman, Zhengnan Huang,
Daniel Rueckert, Florian Knoll, Mehmet Akçakaya

Abstract

Physics-driven deep learning methods have emerged as a powerful tool for computational magnetic resonance imaging (MRI) problems, pushing reconstruction performance to new limits. This article provides an overview of the recent developments in incorporating physics information into learning-based MRI reconstruction. We consider inverse problems with both linear and non-linear forward models for computational MRI, and review the classical approaches for solving these. We then focus on physics-driven deep learning approaches, covering physics-driven loss functions, plug-and-play methods, generative models, and unrolled networks. We highlight domain-specific challenges such as real- and complex-valued building blocks of neural networks, and translational applications in MRI with linear and non-linear forward models. Finally, we discuss common issues and open challenges, and draw connections to the importance of physics-driven learning when combined with other downstream tasks in the medical imaging pipeline.

Index Terms

Accelerated MRI, parallel imaging, iterative image reconstruction, numerical optimization, machine learning, deep learning, physics-driven learning.

K. Hammernik and D. Rueckert are with the Institute of AI and Informatics in Medicine, Technical University of Munich and the Department of Computing, Imperial College London.

T. Küstner is with the Department of Diagnostic and Interventional Radiology, University Hospital of Tuebingen.

B. Yaman and M. Akçakaya are with the Department of Electrical and Computer Engineering, and Center for Magnetic Resonance Research, University of Minnesota, USA.

Z. Huang is with the Center for Biomedical Imaging, Department of Radiology, New York University.

F. Knoll is with the Department Artificial Intelligence in Biomedical Engineering, Friedrich-Alexander University Erlangen.

We acknowledge grant support from the NIH, Grant Numbers: R01HL153146, P41EB027061, R01EB024532 and P41EB017183; from the NSF, Grant Number: CAREER CCF-1651825; and from the EPSRC Programme Grant, Grant Number: EP/P001009/1.

I. INTRODUCTION

Magnetic resonance imaging (MRI) is a non-invasive radiation-free imaging modality with a plethora of clinical applications and extensively-studied physics underpinnings. MRI data is collected in the so-called k-space, corresponding to the spatial Fourier transform of the object's magnetization. More formally, this relationship is given via a linear equation:

$$\mathbf{y} = \mathbf{E}\mathbf{x} + \mathbf{n}, \quad (1)$$

where \mathbf{x} is the image/magnetization of interest, \mathbf{y} denotes the corresponding k-space measurements, \mathbf{E} is the forward MRI encoding operator, and \mathbf{n} is measurement noise. In its simplest form, \mathbf{E} corresponds to a sub-sampled discrete Fourier transform matrix \mathbf{F}_Ω which samples the k-space locations specified by Ω . In practice, however, all clinical MRI scanners from all vendors are equipped with multi-coil receiver arrays, and the corresponding multi-coil forward operator \mathbf{E} is given as

$$\mathbf{E} = \begin{bmatrix} \mathbf{F}_\Omega \mathbf{C}_1 \\ \vdots \\ \mathbf{F}_\Omega \mathbf{C}_{n_c} \end{bmatrix},$$

where n_c is the number of coils in the receiver array, and \mathbf{C}_k is a diagonal matrix containing the sensitivity profile of the k^{th} receiver coil.

Formation of images and other information from these measured k-space data constitutes the basis of computational MRI, which in itself has a rich history [1]. The canonical inverse problem for computational MRI relates to the formation of images from sub-sampled/degraded k-space data. Solving such inverse problems often necessitates incorporation of additional information about MRI encoding and/or the nature of MR images. Earlier works concentrated on the properties of the k-space, such as partial Fourier imaging methods that utilize Hermitian symmetry. With the advent of multi-coil receiver arrays, the redundancies among these coil elements became the important information for the next generation of inverse problems [2]. Subsequently, compressed sensing methods [3] were proposed to utilize the compressibility of MR images, often in addition to the redundancies among the coil elements.

In addition to the above canonical linear inverse problems, there are a class of computational MRI methods that deal with more complicated non-linear forward models incorporating physical, systemic and physiological parameters, such as relaxation [4] or motion [5]. In this case, the forward model is given as

$$\mathbf{y} = \mathcal{E}(\boldsymbol{\vartheta}) + \mathbf{n}, \quad (2)$$

where ϑ are a set of (unknown) parameters that describe the underlying physical or systemic information, and \mathcal{E} is a non-linear encoding operator. Traditionally, such methods are solved using model-based reconstructions.

Recently, deep learning methods have emerged as a powerful tool for solving many inverse problems in computational MRI. Among these, MRI reconstruction for accelerated acquisitions remains the most well-studied [6–8], along with several strategies for quantitative MRI [9], motion [10, 11] and other non-linear physical models [12, 13]. Out of a plethora of approaches for these problems, physics-driven methods have emerged as the most well-received deep learning techniques by the MRI community due to their incorporation of the MR domain knowledge. The goal of this manuscript is to provide a comprehensive review of inverse problems for computational MRI, and how physics-driven deep learning techniques are being used for these applications.

II. CLASSICAL APPROACHES FOR COMPUTATIONAL MRI

The simplest image reconstruction problem for computational MRI concerns the case where \mathbf{E} is exactly the discrete Fourier transform matrix in Eq. (1), corresponding to Nyquist rate sampling for a given resolution and field-of-view. In this case, the image of interest is recovered via inverse discrete Fourier transform.

In practical settings, often a sub-Nyquist rate is employed to enable faster imaging, where the previous simple strategy of taking the inverse Fourier transform leads to aliasing artifacts. Thus, in this regime, an inverse problem, incorporating additional domain knowledge, needs to be solved for image formation. The most commonly used clinical strategy for accelerated MRI is parallel imaging [2], which uses the redundancies among these coil elements for image reconstruction. Succinctly, parallel imaging methods that work in image domain [2] solved

$$\hat{\mathbf{x}}_{PI} = \arg \min_{\mathbf{x}} \frac{1}{2} \|\mathbf{y} - \mathbf{E}\mathbf{x}\|_2^2 = (\mathbf{E}^H \mathbf{E})^{-1} \mathbf{E}^H \mathbf{y}. \quad (3)$$

In theory, with n_c coil elements, the ratio between the image size and the cardinality of Ω , or the acceleration rate (R), can be as high as n_c . However, due to dependencies between $\{\mathbf{C}_k\}$ and ill-conditioning of \mathbf{E} that leads to noise amplification due to the matrix inversion [2], the achievable rates are often limited. Subsequently, compressed sensing methods [3] were proposed to utilize the compressibility of MR images to reconstruct images from sub-sampled k-space data. These methods solve a regularized least squares objective function

$$\hat{\mathbf{x}}_{CS} = \arg \min_{\mathbf{x}} \frac{1}{2} \|\mathbf{y} - \mathbf{E}\mathbf{x}\|_2^2 + \tau \|\mathbf{W}\mathbf{x}\|_1, \quad (4)$$

where $\|\cdot\|_1$ denotes the ℓ_1 norm, \mathbf{W} is a sparsifying linear transform, and τ is a weight term. Unlike (3), this objective function does not have a closed form solution. However, it is a convex problem, and can be solved using numerous iterative algorithms [14].

A. Solving the linear inverse problem in classical computational MRI

In general, we will consider a regularized least squares objective with a broader class of regularizers:

$$\hat{\mathbf{x}}_{reg} = \arg \min_{\mathbf{x}} \frac{1}{2} \|\mathbf{y} - \mathbf{E}\mathbf{x}\|_2^2 + \mathcal{R}(\mathbf{x}), \quad (5)$$

where $\mathcal{R}(\cdot)$ may be one of the aforementioned regularizers, such as the ℓ_1 norm of transform domain coefficients, or implicitly implemented via machine learning techniques, as we will later see.

There is a number of iterative algorithms for solving such objective functions, especially when it is convex [14]. A classical approach, when $\mathcal{R}(\cdot)$ is differentiable, is based on gradient descent:

$$\mathbf{x}^{(i)} = \mathbf{x}^{(i-1)} + \eta \mathbf{E}^H (\mathbf{y} - \mathbf{E}\mathbf{x}^{(i-1)}) - \eta \nabla_{\mathbf{x}} \mathcal{R}(\mathbf{x})|_{\mathbf{x}=\mathbf{x}^{(i-1)}}, \quad (6)$$

where $\mathbf{x}^{(i)}$ is the image of interest at the i^{th} iteration. However, often times nonsmooth regularizers are used in computational MRI. In this case, proximal algorithms are widely used [14]. One such method is proximal gradient descent, which amounts to solving two sub-problems:

$$\mathbf{z}^{(i)} = \arg \min_{\mathbf{z}} \frac{1}{2} \|\mathbf{x}^{(i-1)} - \mathbf{z}\|_2^2 + \eta \mathcal{R}(\mathbf{x}) \triangleq \text{prox}_{\mathcal{R}, \eta}(\mathbf{z}) \quad (7a)$$

$$\mathbf{x}^{(i)} = \mathbf{z}^{(i)} + \eta \mathbf{E}^H (\mathbf{y} - \mathbf{E}\mathbf{z}^{(i)}), \quad (7b)$$

where $\mathbf{x}^{(i)}$ and $\mathbf{z}^{(i)}$ are the image of interest and an intermediate image at the i^{th} iteration respectively, Eq. (7a) corresponds to the so-called proximal operator for the regularizer, Eq. (7b) enforces data consistency, and η is a step size. Note for differentiable \mathcal{R} , proximal gradient descent can be also written in the alternative form:

$$\mathbf{z}^{(i)} = \mathbf{x}^{(i-1)} - \eta \nabla_{\mathbf{x}} \mathcal{R}(\mathbf{x})|_{\mathbf{x}=\mathbf{x}^{(i-1)}} \quad (8a)$$

$$\begin{aligned} \mathbf{x}^{(i)} &= \arg \min_{\mathbf{x}} \frac{1}{2} \|\mathbf{y} - \mathbf{E}\mathbf{x}\|_2^2 + \frac{\eta}{2} \|\mathbf{x} - \mathbf{z}^{(i)}\|_2^2 \\ &= (\mathbf{E}^H \mathbf{E} + \eta \mathbf{I})^{-1} (\mathbf{E}^H \mathbf{y} + \eta \mathbf{z}^{(i)}) \triangleq \text{prox}_{\ell_2, \eta}(\mathbf{z}^{(i)}). \end{aligned} \quad (8b)$$

Another class of popular approaches rely on variable splitting, such as the alternating direction method of multipliers (ADMM), which solves:

$$\mathbf{x}^{(i)} = (\mathbf{E}^H \mathbf{E} + \rho \mathbf{I})^{-1} (\mathbf{E}^H \mathbf{y} + \rho (\mathbf{z}^{(i-1)} - \mathbf{u}^{(i-1)})), \quad (9a)$$

$$\mathbf{z}^{(i)} = \arg \min_{\mathbf{z}} \frac{1}{2} \|(\mathbf{x}^{(i)} + \mathbf{u}^{(i-1)}) - \mathbf{z}\|_2^2 + \frac{1}{\rho} \mathcal{R}(\mathbf{x}), \quad (9b)$$

$$\mathbf{u}^{(i)} = \mathbf{u}^{(i-1)} + (\mathbf{x}^{(i)} - \mathbf{z}^{(i)}), \quad (9c)$$

where $\mathbf{x}^{(i)}$ is the image of interest at the i^{th} iteration, $\mathbf{z}^{(i)}$ and $\mathbf{u}^{(i)}$ are intermediate images, and ρ is a penalty weight. Here, (9a), (9b) and (9c) corresponds to data consistency, proximal operator and dual update sub-problems respectively. A simpler version of ADMM is based on variable splitting with quadratic penalty [14].

B. Solving the non-linear inverse problem in classical computational MRI

A more accurate and complete description of the MR signal model is obtained if other effects like tissue relaxivity, off-resonance, motion, chemical shift, flow, diffusion are taken into account. In this case, the MR signal \mathbf{y}_k at the k^{th} receiver coil, prior to discretization, can be described as

$$\mathbf{y}_k = \int \rho(\mathbf{r}) \mathbf{c}_k(\mathbf{r}) M(\boldsymbol{\vartheta}, \mathbf{x}, t, \mathbf{r}) e^{-j2\pi \mathbf{k}(t) \cdot \mathbf{r}} d\mathbf{r} \quad (10)$$

with spin densities ρ , coil sensitivities \mathbf{c}_k , the signal model $M(\boldsymbol{\vartheta}, \mathbf{x}, t, \mathbf{r})$ of the unknown parameters $\boldsymbol{\vartheta}$, and k-space sampling at spatial points \mathbf{r} defined by the k-space trajectory $\mathbf{k}(t)$.

Based on Eq. 10, the discretized forward operator $\mathcal{E} : \boldsymbol{\vartheta} \rightarrow \mathbf{y}$ becomes non-linear and maps the unknown parameters $\boldsymbol{\vartheta}$ to the measured data \mathbf{y} . It can be decomposed into $\mathcal{E} = \mathbf{E}\mathcal{M}$, where \mathbf{E} is the canonical forward operator and \mathcal{M} is the signal model describing the spin physics [4]. Given a reconstructed image series \mathbf{x} , a parametric fitting can be performed by a least-squares minimization

$$\hat{\boldsymbol{\vartheta}} = \arg \min_{\boldsymbol{\vartheta}} \|\mathcal{M}(\boldsymbol{\vartheta}) - \mathbf{x}\|_2^2 \quad (11)$$

that fits the image series into the defined signal model \mathcal{M} parametrized by $\boldsymbol{\vartheta}$ [4].

Alternatively, the signal model can be directly incorporated into the image reconstruction, i.e. the unknown parameters $\boldsymbol{\vartheta}$ are estimated from the acquired data \mathbf{y} without having to reconstruct individual images first, based on model-based reconstruction. The general unconstrained optimization problem for a model-based reconstruction with a class of regularizers $\{R_i(\cdot)\}$ on the underlying unknown parameters $\boldsymbol{\vartheta}$ can be stated as:

$$\hat{\boldsymbol{\vartheta}} = \arg \min_{\boldsymbol{\vartheta}} \|\mathcal{E}(\boldsymbol{\vartheta}) - \mathbf{y}\|_2^2 + \sum_i \lambda_i R_i(\boldsymbol{\vartheta}). \quad (12)$$

In contrast to parametric fitting, intermediate image reconstruction is not necessary for model-based reconstructions, and the parameters of interest can be directly estimated (under the assumption of a complete signal model description). This description is very general and combines parallel imaging, compressed sensing and model-based reconstruction in a unified formulation. The individual factors that form the forward operator can either be pre-computed, are known, or can be estimated as unknowns. For the inverse problems with non-linear forward operators, the algorithms are less standardized, and typically application-dependent. Eq. (12) is usually non-convex, making its optimization a challenging

task. Furthermore, inaccuracies or incompleteness of the modelled parameters can further influence the optimization. One approach is to employ Gauss-Newton algorithm, and linearize the problem around the solution of the previous iteration [1] or by approximating the non-linear behaviour with a linear combination of basis functions [15].

III. PHYSICS-DRIVEN ML METHODS IN COMPUTATIONAL MRI

Deep learning methods have recently emerged as a powerful tool for computational MRI. These methods can be broadly split into two classes: purely data-driven and physics-driven [16]. The former methods are typically implemented in image space, as removing artifacts from aliased images [17]. These image enhancement networks are typically trained to map corrupted and undersampled images to artifact-free images. Indeed, learning image enhancement networks is the key ingredient to remove artifacts in image domain. However, when only image enhancement methods are used, the information of the acquisition physics is entirely discarded, hence, k-space consistency cannot be guaranteed. In this section, we will give an extensive overview on physics-driven deep learning methods for computational MRI, ranging from physics-informed enhancement methods to learned unrolled optimization, as well as reconstruction with generative models and plug-and-play priors.

A. *Physics Information in Image/k-space Enhancement Methods*

As aforementioned, image enhancement networks typically learn a mapping from the aliased/degraded image, such as the zero-filled reconstruction, to a reference image, without consideration of the measured k-space data during the reconstruction process. Several attempts have been made to incorporate physics information in this line of work, including enforcing k-space consistency directly after image enhancement [18], or adding k-space consistency as an additional cost function term during training [19]. The former approach directly replaces the measured k-space lines, which may lead to artifacts, while the latter cannot guarantee k-space consistency during inference, especially for cases with unseen pathologies. Similarly, enhancement has been proposed in k-space, as a method of interpolation [20], where a non-linear interpolation function is learned from calibration data. This can be seen as an extension to the linear convolution kernels used in parallel imaging [8]. As only the calibration data is required for training, this approach can be used when large training databases are not available, but its performance may be limited at high acceleration rates where the calibration data may be insufficient [8].

B. *Plug-and-play Methods with Deep Denoisers*

Plug-and-play (PnP) algorithms decouple image modeling from the physics of the MRI acquisition, by noting that the proximal operators in Eq. (7a) or Eq. (9b) correspond to conventional denoising

problems [21]. In the proximal-based formulation, these proximal denoisers are replaced by other powerful denoising algorithms, which do not necessarily have a corresponding closed form $\mathcal{R}(\cdot)$ expression, such as BM3D [21]. A related approach is the regularization by denoising (RED) framework, which considers finding \mathbf{x} that solves the optimality condition

$$\mathbf{0} = \mathbf{E}^H(\mathbf{E}\mathbf{x} - \mathbf{y}) + \nu(\mathbf{x} - d(\mathbf{x})), \quad (13)$$

where $d(\cdot)$ is the plug-in denoiser [21]. The advantage of the RED formulation is that under certain conditions, the regularizer, $\mathcal{R}(\cdot)$ can be explicitly tied to the denoiser, $d(\cdot)$, on which more explanations are detailed in a previous review article [21].

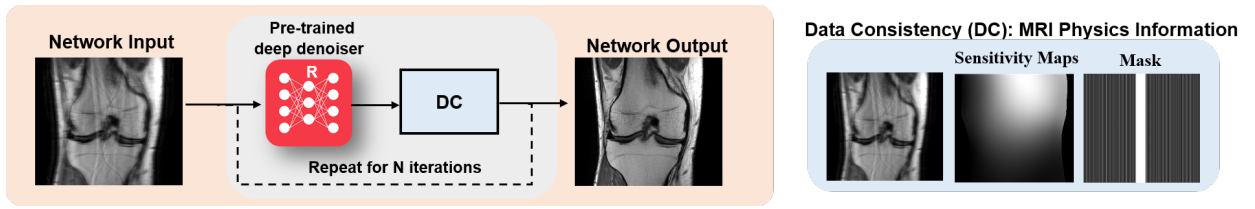


Fig. 1: Overview of the PnP framework in physics-driven deep learning methods for computational MRI. The data consistency unit enforces fidelity with k-space measurements based on the known forward model.

Recently, more effort has been made towards implementing CNN-based denoisers in these PnP frameworks [21–23], depicted in Figure 1. These denoisers are typically trained using reference images in a supervised manner, where different levels of noise are retrospectively added to these images, and a mapping from the noisy images to reference images are learned [21]. In applications, where reference images are unavailable, denoising frameworks have been proposed for training using pairs of noisy images [24]. Extending on these works, regularization by artifact removal (RARE) trained CNN denoisers on a database of pairs of images with artifacts generated from non-Cartesian acquisitions [22]. These pairs were generated by splitting the acquired measurements in half, and reconstructing these with least squares as in Eq.(3), corresponding to a parallel imaging reconstruction, which led to starting images of sufficient quality for non-Cartesian trajectories that oversample the central k-space. The appeal of these methods is that the CNN-based denoisers are trained independent of the broader inverse problem. Thus, only the denoising network has to be stored in memory, allowing for easier translation to larger-scale, e.g. 3D MRI datasets [22]. This approach is also appealing since only one denoiser has to be trained on any data. Hence, this denoiser can, in principle, be applied across different rates or undersampling patterns. In practice, it is beneficial to provide the denoiser with additional information, such as the undersampling artifacts arising from uniform undersampling pattern in order to recognize characteristic aliasing artifacts.

C. Generative Models

While we have reviewed explicit regularization in Eq. (5), regularization can also be achieved by an implicit prior in order to constrain the solution space for our optimization problem. This concept is proposed by Deep Image Prior (DIP) [25] as follows:

$$\min_{\boldsymbol{\theta}} \frac{1}{2} \|\mathbf{E}G(\mathbf{z}, \boldsymbol{\theta}) - \mathbf{y}\|_2^2,$$

where a generator network, G parametrized by $\boldsymbol{\theta}$, reconstructs an image from a random latent vector \mathbf{z} . This loss function is used to train the generator network with parameters $\boldsymbol{\theta}$. This formulation has the advantage that it works for limited (even single) datasets without ground-truth. However, early stopping has to be performed to not overfit to the noisy measurement data. While DIP methods were originally proposed for general inverse problems such as denoising, superresolution and deblurring, its application to MRI reconstruction has also been studied [26], where the zero-filled reconstruction was used instead of the latent code as an input to the generator UNet. An extension of the DIP framework to dynamic non-cartesian MRI was proposed in [27]. Starting from a noise vector, a mapping network first generated an expressive latent space from a fixed low-dimensional manifold, using fully connected layers and non-linearities. A subsequent generative CNN generates the finally reconstructed image. A wavelet-sparsity constraint on the generated image was added as regularization to Eq. (16), to improve the efficiency of learning and avoid over-fitting to the noisy measurement data, and was further conditioned with a high-resolution image of similar anatomy [28].

An alternative line of work is based on generative adversarial networks (GANs), where a generator and a discriminator network play a minimax game. The generator network samples from a fixed distribution in latent space such as Gaussian distribution and aims to map the sampling to a real data distribution in ambient image space. Conversely, the discriminator network aims to differentiate between generated and real samples. The minimax training objective is defined as

$$\min_{\boldsymbol{\theta}_G} \max_{\boldsymbol{\theta}_D} \mathcal{L}_{GAN}(\boldsymbol{\theta}_D, \boldsymbol{\theta}_G) \triangleq \mathbb{E}_{\mathbf{x}}[\log D(\mathbf{x}, \boldsymbol{\theta}_D)] + \mathbb{E}_{\mathbf{z}}[\log(1 - D(G(\mathbf{z}, \boldsymbol{\theta}_G), \boldsymbol{\theta}_D))], \quad (14)$$

where the distribution on \mathbf{x} is the real data distribution, whereas the one on \mathbf{z} is a fixed distribution on the latent space. The generator G , parametrized by $\boldsymbol{\theta}_G$, tries to map samples from the latent space to samples from the ambient image space, and the discriminator D , parametrized by $\boldsymbol{\theta}_D$, tries to differentiate between the generated and the real samples. The idea of using GANs in computational MRI was first proposed in [29]. In this case, the generator network used the zero-filled images as input instead of a random distribution, leading to the loss function

$$\min_{\boldsymbol{\theta}_G} \max_{\boldsymbol{\theta}_D} \mathbb{E}_{\mathbf{x}}[\log D(\mathbf{x}, \boldsymbol{\theta}_D)] + \mathbb{E}_{\mathbf{z}}[\log(1 - D(G(\mathbf{E}^H \mathbf{y}, \boldsymbol{\theta}_G), \boldsymbol{\theta}_D))], \quad (15)$$

and \mathcal{G} was in essence an image enhancement network, followed by a data consistency step. A high-level overview of this approach is shown in Figure 2. A more recent work replaced this generator with a variational autoencoder based generator that also allowed for uncertainty quantification [30].

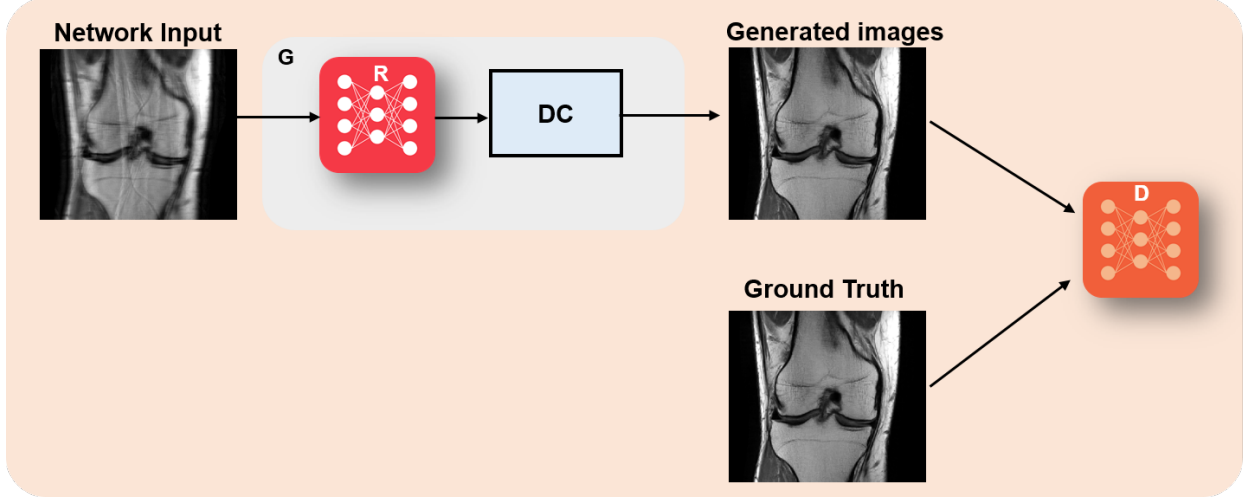


Fig. 2: Overview of GAN methods in physics-driven deep learning methods for computational MRI. In the unsupervised setting, such as cycleGANs, physics information is further enforced in the loss function both in image and k-space domains.

Another approach is based on inverse GANs, which utilize generative learning, followed by optimization similar to the DIP [31]. First, a GAN is trained to generate MR images from a latent noise vector. The GAN does not involve any physics-based knowledge, as only clean MRI reference images are used for training. The physics-based information is then included in a refinement step, where both the generator parameters and the latent vector are optimized following:

$$\min_{\theta, \mathbf{z}} \frac{1}{2} \|\mathbf{E}G(\mathbf{z}, \theta) - \mathbf{y}\|_2^2, \quad (16)$$

This allows for adaptation of the generator to the undersampled k-space data at test time, and is not restricted to any sampling pattern.

Within the GAN framework, much work has been done to adapt GANs into a setting that does not require paired input and label data for computational MRI. In an important line of work, cycle consistent GANs (cycleGAN), which enable unpaired image-to-image translation, have been analyzed using optimal transport, which provides a means to transport probability measures by minimizing average transport between measures [32]. While traditional GANs and DIP-like networks are based on minimizing the statistical distance in k-space, CycleGAN aims to minimize this in both k-space and image domain. In

essence, this is achieved by minimizing two forms of losses, one for cyclic consistency and one for GAN training. The former is

$$\mathcal{L}_{\text{cycle}}(\boldsymbol{\theta}_G) = \mathbb{E}_{\mathbf{x}}[\|\mathbf{x} - G(\mathbf{y}, \boldsymbol{\theta}_G)\|_2^2] + \mathbb{E}_{\mathbf{x}}[\|\mathbf{y} - \mathbf{E}G(\mathbf{y}, \boldsymbol{\theta}_G)\|_2^2], \quad (17)$$

where the generator uses k -space measurements \mathbf{y} as input. Here, the first term ensures consistency in the image domain, while the latter enforces consistency in the k -space domain. The second part of the training loss is a Wasserstein GAN loss, $\mathcal{L}_{\text{WGAN}}(\boldsymbol{\theta}_G, \boldsymbol{\theta}_D)$ which is a generalization of Eq. (14) with improved training stability [32]. The final training loss is given as a weighted combination of these

$$\mathcal{L}_{\text{cycleGAN}} = \gamma \mathcal{L}_{\text{cycle}}(\boldsymbol{\theta}_G) + \mathcal{L}_{\text{WGAN}}(\boldsymbol{\theta}_G, \boldsymbol{\theta}_D), \quad (18)$$

where γ is a weighting hyperparameter. This approach was shown to enable unsupervised training of generative models for improved MRI reconstruction [32].

D. Algorithm unrolling and unrolled networks

Algorithm unrolling considers the traditional iterative approaches considered in Section II-A and adapts them in a manner that is amenable to learning the optimal parameters for image reconstruction [16]. Traditional approaches require numerous iterations during optimization to solve the MRI reconstruction problem. Additionally, only a fixed, handcrafted regularizer is used, which do not necessarily model MR images accurately. Instead of solving a new optimization problem for each task, the whole iterative reconstruction procedure, including the image regularizer, can be learned. The original idea was proposed in the context of sparse coding [33], but has found great use in computational imaging applications, including computational MRI. In this line of work, a conventional iterative algorithm for solving Eq. (5) is unrolled and solved for a fixed number of iterations, as overviewed in Figure 3. In practice, any iterative optimization algorithm can be unrolled for solving Eq. (5). In the context of MRI, algorithm unrolling is based on ADMM [34] as described in Eq. (9a)-(9c), gradient descent schemes [6], proximal gradient schemes [7, 35, 36], primal-dual methods [37], or variable splitting methods [38–40].

Variational Networks (VNs) are an example for an unrolled gradient descent scheme. In this method, the gradient descent approach in Eq. (6) is unrolled for N_i steps. In VNs, the gradient with respect to the regularizer $\nabla_{\mathbf{x}} \mathcal{R}(\mathbf{x})|_{\mathbf{x}=\mathbf{x}^{(i-1)}}$ is derived from the Fields-of-Experts (FoE) regularizer [41], i.e.,

$$\mathcal{R}(\mathbf{x}) = \sum_{j=1}^{N_k} \langle \Phi_j(\mathbf{K}_j \mathbf{x}), \mathbf{1} \rangle,$$

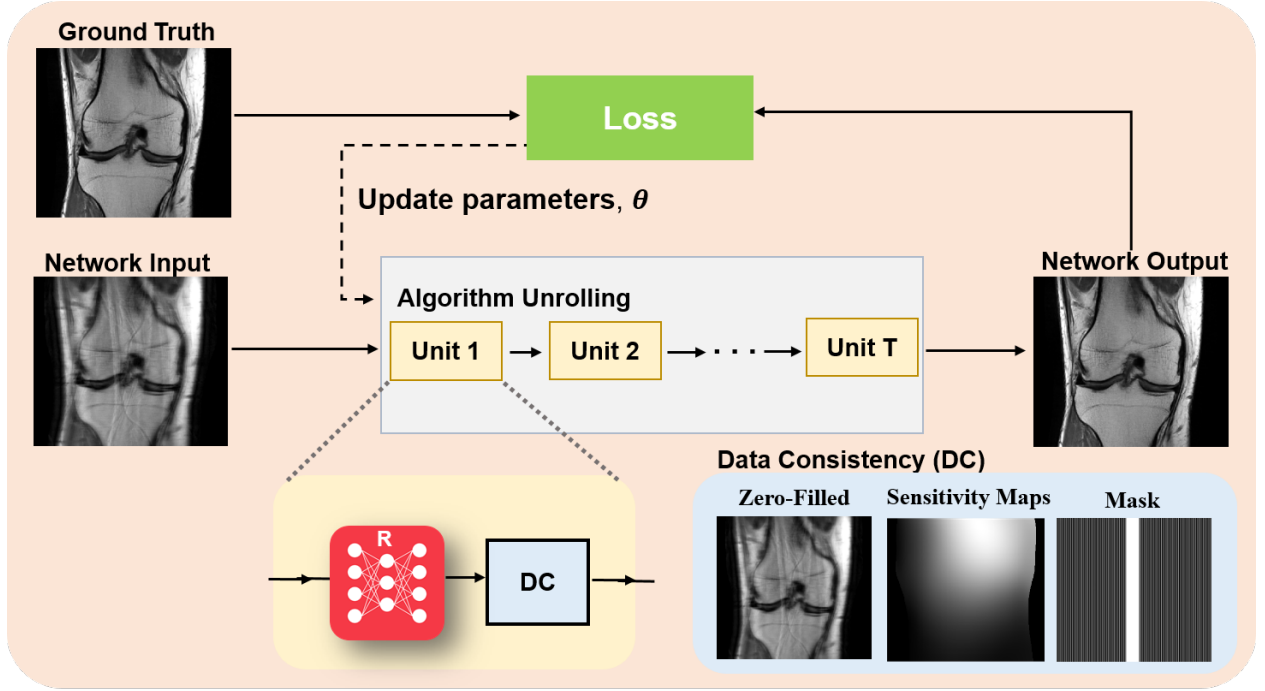


Fig. 3: Overview of algorithm unrolling in physics-driven deep learning methods for computational MRI. An iterative algorithm for solving Eq. (5) is unrolled for a fixed number of iterations, and trained end-to-end using appropriate labels.

where $\mathbf{1}$ denotes a vector of ones. This can be seen as a generalization of the Total Variation semi-norm for a number of N_k convolution operators \mathbf{K} and non-linear potential functions Φ . Calculating the gradient with respect to \mathbf{x} yields:

$$\nabla \mathcal{R}(\mathbf{x})|_{\mathbf{x}=\mathbf{x}^{(i-1)}} = \sum_{j=1}^{N_k} \mathbf{K}_j^H \Phi'_j(\mathbf{K}_j \mathbf{x}), \quad (19)$$

where Φ' denotes trainable activation functions. The small number of trainable parameters make VNs easy to train and fast to run. VNs are characterized by the energy-based formulation of the regularizer. In the context of MRI reconstruction, the FoE model [6] and the Total Deep Variation model [42] are proposed for energy-based regularization. In other approaches, this energy-based formulation is discarded and the gradient with respect to \mathbf{x} is replaced by a CNN with trainable parameters θ :

$$\nabla \mathcal{R}(\mathbf{x})|_{\mathbf{x}=\mathbf{x}^{(i-1)}} = \text{CNN}_{\theta}(\mathbf{x}^{(i-1)}). \quad (20)$$

In the context of learned gradient descent schemes, multi-scale regularizers such as UNET [43], or Down-Up Networks [44] are commonly used.

Another line of work considers the proximal gradient descent scheme from either Eq. (7a)-(7b) or Eq. (8a)-(8b). The latter approach was used in data consistent CNNs [35] and MoDL [7], which again replace the gradient with respect to \mathbf{x} by a CNN with trainable parameters $\boldsymbol{\theta}$ as in Eq. (20). This leads to the following scheme:

$$\mathbf{z}^{(i)} = \mathbf{x}^{(i-1)} - \text{CNN}_{\boldsymbol{\theta}}(\mathbf{x}^{(i-1)}) \quad (21a)$$

$$\mathbf{x}^{(i)} = (\mathbf{E}^H \mathbf{E} + \eta \mathbf{I})^{-1} (\mathbf{E}^H \mathbf{y} + \eta \mathbf{z}^{(i)}), \quad (21b)$$

where η is an additional learnable parameter. The proximal mapping in Eq. (21b) can be solved as closed-form solution as proposed in [35] for single-coil datasets, or using an iterative optimization approach based on conjugate gradient (CG) [7] for the more commonly used multi-coil setup. Note in this case, the CG algorithm itself has to be unrolled for a fixed number of iterations for easy back-propagation through the whole network. Once again, the CNN in Eq. (21a) can be any kind of regularization network, as the idea is agnostic to the particulars of the CNN that is used in this step.

The alternative form of proximal gradient descent unrolling utilizes Eq. (7a)-(7b), and leads to the replacement of the proximal operator of $\mathcal{R}(\cdot)$ by a CNN with trainable parameters $\boldsymbol{\theta}$, leading to:

$$\mathbf{z}^{(i)} = \text{CNN}_{\boldsymbol{\theta}}(\mathbf{x}^{(i-1)}) \quad (22a)$$

$$\mathbf{x}^{(i)} = \mathbf{z}^{(i)} + \eta \mathbf{E}^H (\mathbf{y} - \mathbf{E} \mathbf{z}^{(i)}). \quad (22b)$$

This method was utilized in [45]. This approach leads to a less memory intensive data consistency step in Eq. (22b) compared to Eq. (21b), especially for multi-coil datasets, but its performance lags the CG approach used in MoDL [40].

1) Training unrolled networks: The output of the unrolled network depends on the variables in both the regularization and data consistency units, and can be represented with a function $f_{\text{unroll}}(\mathbf{y}, \mathbf{E}; \{\boldsymbol{\theta}_i, \eta_i\}_{i=1}^{N_t})$, where for the most generalized representation, we allow the regularizer CNN parameters $\boldsymbol{\theta}$ and the data consistency parameters η to vary across the unrolled iterations. While for ease of notation, we have referred to the multi-coil operator as \mathbf{E} , this operator implicitly includes the sub-sampling mask Ω . For the following, we will make this dependence explicit, and use \mathbf{E}_{Ω} and \mathbf{y}_{Ω} for the multi-coil operator and the measured k-space data, respectively.

The standard learning strategy for unrolled networks is to train them end-to-end, using the full network that has been unrolled for N_t steps. For end-to-end training of unrolled networks, the most commonly used paradigm relies on supervised learning, where a database of fully-sampled measurements/ground-truth images as a reference. Given a database of pairs of input and reference data, the supervised learning loss function can be written as

$$\min_{\{\boldsymbol{\theta}_i, \eta_i\}_{i=1}^{N_t}} \frac{1}{N} \sum_{n=1}^N \mathcal{L}(\mathbf{x}_{\text{ref}}^n, f(\mathbf{y}_{\Omega}^n, \mathbf{E}_{\Omega}^n; \{\boldsymbol{\theta}_i, \eta_i\}_{i=1}^{N_t})), \quad (23)$$

where $\boldsymbol{\theta}$ represents the network parameters, N is the number of samples in the training database, $\mathcal{L}(\cdot, \cdot)$ is a loss function characterizing the difference between network output and referenced data, $\mathbf{x}_{\text{ref}}^n$ denotes the ground-truth image for subject n . The domain for the loss function can be image, k-space or a mixture of them. Numerous loss functions such as ℓ_1 , ℓ_2 , adversarial and perceptual losses have been used in supervised deep learning approaches [8].

However, in many applications, fully-sampled reference data may be impossible to acquire, for instance due to organ motion or signal decay, or may be impractical due to excessively long scan times. In these cases, self-supervised learning enables training of neural networks without fully-sampled data by generating training labels from the sub-sampled measurements themselves [46]. One of the first works in this area, self-supervised learning via data undersampling (SSDU) [39], partitions the acquired measurements Ω , for each scan into two disjoint sets, Θ and Λ . One of these sets, Θ , is used during training to enforce data consistency within the network, while the other set, Λ , remains unseen by the unrolled network and is used to define the loss function in k-space. Hence, SSDU performs end-to-end training by minimizing the following self-supervised loss:

$$\min_{\boldsymbol{\theta}} \frac{1}{N} \sum_{n=1}^N \mathcal{L}(\mathbf{y}_{\Lambda}^n, \mathbf{E}_{\Lambda}^n(f(\mathbf{y}_{\Theta}^n, \mathbf{E}_{\Theta}^n; \boldsymbol{\theta}))), \quad (24)$$

where the network output is transformed back to k-space by applying the encoding operator \mathbf{E}_{Λ}^n at unseen locations in training. Thus, the self-supervised loss function measure the reconstruction quality of the model by characterizing the discrepancy between the unseen acquired measurements and network output measurements at the corresponding locations. After the network is trained, the reconstruction for unseen test data is performed by using all acquired measurements Ω . In another line of work [47], Stein's unbiased risk estimate of mean square error (MSE) is leveraged to enable unsupervised MRI reconstruction. In particular, the loss function obtained from an ensemble of images, each acquired by employing different undersampling operator, has been shown to be an unbiased estimator for MSE.

Finally, like generative models based on DIP, there has been interest in training unrolled networks on single datasets without a database. In this setting, the number of trainable parameters is usually larger than the number of pixels/k-space measurements, and training may lead to overfitting. Recent work in this area has tackled this challenge by developing a zero-shot self-supervised learning [48] approach that includes a third additional partition, which is used to monitor a self-validation loss in addition to the previous self-supervision setup. This self-validation loss starts to increase once overfitting is observed.

Once the model training is stopped, the final reconstruction is calculated by performing a forward pass at stopping epoch using all acquired measurements.

2) *Memory challenges of unrolled networks*: A major challenge for training unrolled networks is their large memory footprint. When an algorithm is unrolled for N_t iterations, a straightforward implementation involves the storage of N_t CNNs, along with N_t DC operations in GPU memory. The latter itself can have a large footprint, when a CG-type approach is used [7]. This creates challenges for training unrolled networks for large-scale or multi-dimensional datasets. Recently, this was tackled with the development of memory-efficient learning schemes [49]. In memory-efficient learning, intermediate outputs from each unrolled iteration are stored on host memory during forward pass, and backpropagation gradients are computed using this intermediate data and gradients from the preceeding step. Thus, this approach conceptually supports as many unrolling steps as desired, with the drawback of additional data transfer between GPU and the host memory.

Another alternative for handling the large memory footprint of unrolled networks is deep equilibrium networks [50]. These networks solve a fixed point equation for an operator corresponding to a single unroll, which leads to two advantages for training. First, only one unroll has to be stored during training, leading to a smaller memory usage. Second, the converge behavior for different values of N_t during inference is more well-behaved compared to unrolled networks, which are designed to achieve maximal performance for a specific value of N_t . On the other hand, deep equilibrium networks are run until convergence and do not have fixed inference time unlike unrolled networks, which may not be ideal in clinical applications.

IV. STATE-OF-THE-ART IN MRI PRACTICE AND DOMAIN-SPECIFIC CHALLENGES

A. *Real vs complex building blocks*

As complex-valued data is used in computational MRI, this has to be considered in the network processing pipeline, not only during data consistency, but also in the network blocks itself. Two processing modes are possible: 1) Real/Imaginary or magnitude/phase are considered in two input channels stacked via the feature dimension, 2) Complex-valued operations are performed on complex-valued tensors. While the former allows us to use real-valued operations, the complex relationship between real and imaginary parts is lost. Complex-valued operations maintain the complex nature of the data, but some operations require twice the amount of trainable parameters. For example in complex-valued convolutions, a real and imaginary filter kernel needs to be learned. Additionally, the number of multiplications doubles compared to real-valued processing. If complex-valued layers and tensors are involved, complex back-propagation following Wirtinger calculus has to be considered [51, 52] which is supported in most recent frameworks

(Tensorflow \geq v1.0, PyTorch \geq v1.10). An overview of the most common layer operations together with their complex-valued Wirtinger derivatives is shown in Table I. In the context of MRI reconstruction, complex-valued processing is conducted in both ways.

TABLE I: Overview of important functions along with their pair of Wirtinger derivatives.

Function	$f(\mathbf{x})$	$\frac{\partial f}{\partial \mathbf{x}}$	$\frac{\partial f}{\partial \mathbf{x}^H}$
Magnitude	$ \mathbf{x} = (\mathbf{x}^H \mathbf{x})^{0.5}$	$\frac{\mathbf{x}^H}{2f(\mathbf{x})}$	$\frac{\mathbf{x}}{2f(\mathbf{x})}$
Phase	$-\mathrm{i} \log \frac{\mathbf{x}}{ \mathbf{x} }$	$-\frac{\mathrm{i}}{2\mathbf{x}}$	$\frac{\mathrm{i}}{2\mathbf{x}^H}$
Real Component	$\frac{1}{2} (\mathbf{x} + \mathbf{x}^H)$	$\frac{1}{2}$	$\frac{1}{2}$
Imaginary Component	$\frac{1}{2\mathrm{i}} (\mathbf{x} - \mathbf{x}^H)$	$\frac{1}{2\mathrm{i}}$	$\frac{\mathrm{i}}{2}$
Normalization	$\frac{\mathbf{x}}{(\mathbf{x}^H \mathbf{x})^{0.5}}$	$\frac{1}{2(\mathbf{x}^H \mathbf{x})^{0.5}}$	$-\frac{z^2}{2(\mathbf{x}^H \mathbf{x})^{1.5}}$
Scalar product	$\mathbf{w}^H \mathbf{x}$	\mathbf{w}^H	0
Max Pooling	$\mathbf{x}_n, n = \arg \max_k \mathbf{x}_k $	$\begin{cases} 1 & \text{if } n = \arg \max_k \mathbf{x}_k \\ 0 & \text{else} \end{cases}$	0
Dropout	$\begin{cases} \frac{1}{p} \mathbf{x}_n & \text{if } n \in \Omega \\ 0 & \text{else} \end{cases}$	$\begin{cases} \frac{1}{p} & \text{if } n \in \Omega \\ 0 & \text{else} \end{cases}$	0
Separable activation			
(ReLU, Sigmoid, ...)	$f(\mathrm{Re}(\mathbf{x})) + \mathrm{i}f(\mathrm{Im}(\mathbf{x}))$	$\frac{1}{2} \left(\frac{\partial f}{\partial \mathbf{x}}(\mathrm{Re}(\mathbf{x})) + \frac{\partial f}{\partial \mathbf{x}}(\mathrm{Im}(\mathbf{x})) \right)$	$\frac{1}{2} \left(\frac{\partial f}{\partial \mathbf{x}}(\mathrm{Re}(\mathbf{x})) - \frac{\partial f}{\partial \mathbf{x}}(\mathrm{Im}(\mathbf{x})) \right)$
Cardioid [51]	$\frac{1}{2} (1 + \cos(\angle \mathbf{x})) \mathbf{x}$	$\frac{1}{2} + \frac{1}{2} \cos(\angle \mathbf{x}) + \frac{\mathrm{i}}{4} \sin(\angle \mathbf{x})$	$-\frac{\mathrm{i}}{4} \sin(\angle \mathbf{x}) \frac{\mathbf{x}}{\mathbf{x}^H}$
Complex sigmoid	$\frac{1}{1+e^{-z}}$	$\frac{e^{-z}}{(1+e^{-z})^2}$	0

1) *Convolution:* The discrete convolution maps the $N_{f,\mathrm{in}}$ input feature channels to $N_{f,\mathrm{out}}$ output feature channels of an image $\mathbf{x} \in \mathbb{K}$ with filter kernels $\mathbf{k}_{i,j} \in \mathbb{K}$ via

$$\hat{\mathbf{x}}_j = \sum_{i=1}^{N_{f,\mathrm{in}}} \mathbf{x}_i * \mathbf{k}_{i,j} \quad j = 1, \dots, N_{f,\mathrm{out}}, \quad (25)$$

where the subscripts denote the feature channels. For real-valued convolutions it is $\mathbb{K} = \mathbb{R}$. For complex convolutions, $\mathbb{K} = \mathbb{C}$, the convolution operation is extended to

$$\begin{aligned} \mathbf{x}_i * \mathbf{k}_{i,j} &= (\mathrm{Re}(\mathbf{x}_i) * \mathrm{Re}(\mathbf{k}_{i,j}) - \mathrm{Im}(\mathbf{x}_i) * \mathrm{Im}(\mathbf{k}_{i,j})) \\ &\quad + \mathrm{i} \cdot (\mathrm{Im}(\mathbf{x}_i) * \mathrm{Re}(\mathbf{k}_{i,j}) + \mathrm{Re}(\mathbf{x}_i) * \mathrm{Im}(\mathbf{k}_{i,j})) \end{aligned} \quad (26)$$

2) *Activation:* When applying non-linear activation functions ϕ to complex values, the impact on magnitude and phase information needs to be considered. One possibility is to apply the activation function to the real and imaginary part separately as separable activations, however, the natural correlation

between real and imaginary channels are not considered in this case. Furthermore, phase information is mapped to the first quadrant, i.e., the interval $[0, \frac{\pi}{2}]$. Alternative approaches have been proposed that retain phase information, for example siglog. As another option, the phase information can be fixed and only the magnitude information is altered by the activation. An example therefor is the *ModReLU*

$$\phi_{\text{ModReLU}}(\mathbf{x}) = \max(0, |\mathbf{x}| + \beta) \frac{\mathbf{x}}{|\mathbf{x}|} \quad (27)$$

where β is the bias that is trainable. A new complex activation function called *Cardioid* was also proposed for MRI processing [51]

$$\phi_{\text{Cardioid}}(\mathbf{x}) = \frac{1}{2} (1 + \cos(\angle \mathbf{x} + \beta)) \mathbf{x} \quad (28)$$

The complex cardioid can be seen as a generalization of ReLU activation functions to the complex plane. Compared to other complex activation functions, the complex cardioid acts on the input phase rather than the input magnitude. A bias β can be additionally learned.

3) *Normalization*: Adding normalization layers (batch, instance or layer/group normalization) directly after convolution layers are a common way to enable faster and more stable training of networks. Statistics are estimated from the input and used to re-parametrize the input. Complex-valued normalization layers require to estimate the normalization via the covariance matrix [52] and are straight-forward to implement. The subsequent layers are less tolerant to changes in previous layers. The selection of the normalization layer is task dependent. Although normalization layers are often important to train a network, they might lead to unwanted artifacts for image restoration tasks [53].

4) *Pooling*: Pooling layers are used as down-sampling operation to reduce the spatial resolution in the image and to introduce approximate invariance to small translations. Small patches are analyzed in the individual features maps to keep important information about extracted features. Common pooling layers are *Average Pooling* and *Max Pooling*. For complex-valued images, the maximum operation does not exist. Instead, the pooling layer is modified such that it keeps values with, e.g., the maximum magnitude response.

B. Canonical MRI reconstruction with the linear forward model

Physics-driven MRI deep learning methods have become the most popular approach in computational MRI due to their improved robustness, especially for the accelerated MRI problem that relies on the linear forward model in Eq. (1). Such methods have been the top performers in community-wide reconstruction challenges, such as the fastMRI challenge [54, 55]. Indeed, the difference between the state-of-the-art algorithms for the fastMRI challenge is hardly visible for the different undersampling factors. These

algorithms have in common that data consistency is included, and expressive regularization networks are used. Imaged pathologies do not necessarily be included in the training dataset, as long as the acceleration factors is not pushed too far and the pathologies are encoded in the k-space [56].

However, even physics-driven deep learning methods face some challenges for accelerated MRI. The impact of domain shift, i.e., training and testing on different data was studied in [44], for different acceleration factors. All training and evaluation is based on the fastMRI knee and neuro datasets [54]. While for acceleration 4, the proposed Down-Up networks with varying data consistency layers generalize well for both anatomies, the type and amount of training data becomes more critical for acceleration factor 8. Since fewer data is available for data consistency at this acceleration, the networks start to reconstruct anatomical structures that are not real. When trained on a subset of knee data and applied to neuro data, the ventricles start resembling knee structures, for acceleration 8 as depicted in Figure 4.

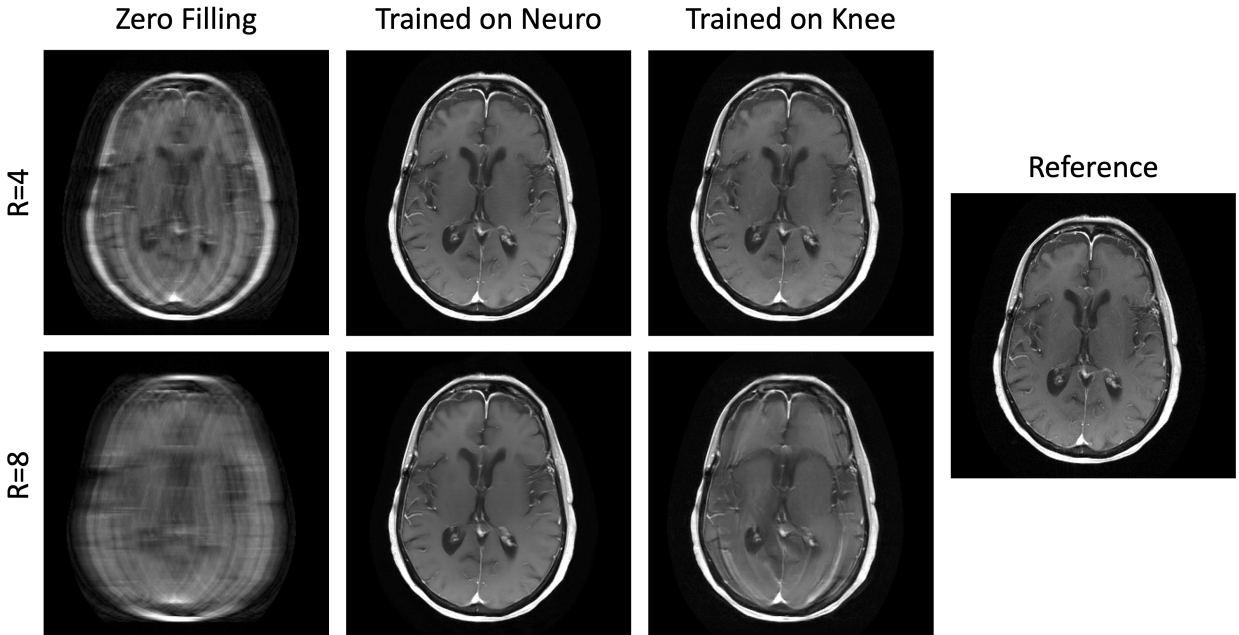


Fig. 4: Down-Up Networks combined with a proximal mapping layer for data consistency [44], trained with different data configuration. While the reconstruction performance generalizes well independent of the type of training data for $R=4$, the ventricles of the brain change here when trained with the wrong data, i.e., knee data for $R=8$.

All previously mentioned approaches consider the complex-valued MR images as images with two real-valued feature channels. CINENet [57] combined both data consistency layers with complex-valued building blocks as depicted in Figure 5, for dynamic 3D ($3D+t$) data. These complex-valued building blocks include convolutions, activations, pooling, and normalization layers. To process the $3D+t$ in the

regularization network, convolution operations are split into 3D spatial convolutions, followed by 1D temporal convolutions.

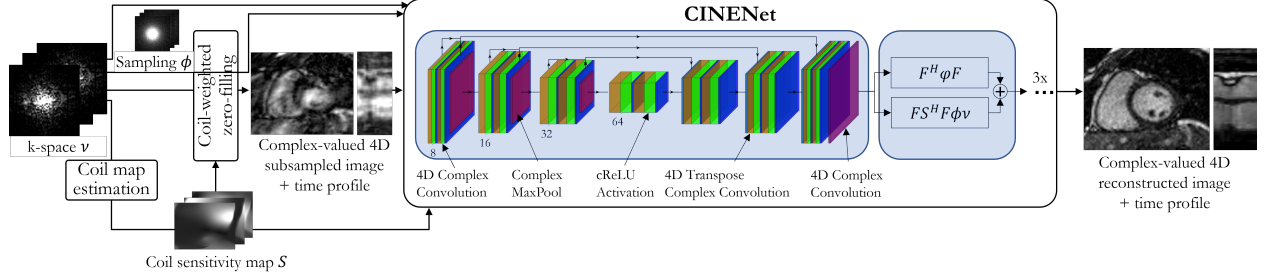


Fig. 5: CINENet combines data consistency layers and a UNet architecture with complex-valued building blocks for convolution, activation, normalization and pooling layers. To process the $3D+t$ data, convolutions are split into 3D spatial convolutions and 1D temporal convolutions.

Finally, as aforementioned the need for fully-sampled data for training had hindered the use of deep learning reconstructions for certain applications. Thus, alternative methods have been explored. Dynamic contrast-enhanced MRI (DCE-MRI) represents one such challenging acquisition, where k -space data is acquired continuously while contrast agent been injected to the patient. The dynamic distribution of the contrast agent causes the image contrast dynamics, hence, both the k -space and image are time-series. In this setting, a variational network was trained on simulated data with radial k -space trajectories, as fully sampled dataset with both high spatial and temporal resolution was infeasible to acquire [58]. With the recent advances outlined in Section III-D1, training in such scenarios can also be done in with more realistic datasets without resorting to simulations. For instance, in another contrast-based cardiac acquisition, called late gadolinium enhancement imaging, unrolled networks have been trained using prospectively accelerated acquisitions without reference data [59], and were shown to improve on clinically used compressed sensing methods, doubling the achievable acceleration rates, as depicted in Figure 6.

C. Inverse problems in MRI with non-linear forward models

Recently, deep learning models have been proposed to address the computationally demanding task of non-linear inverse problems in MRI. An end-to-end formulation towards Eq. 12 is obtained if the learning objective is stated as a maximum likelihood estimation. A neural network mapping $f_{\text{NM}}(\mathbf{x}, \boldsymbol{\theta}) : \mathbf{x} \rightarrow \boldsymbol{\vartheta}$, parametrized by $\boldsymbol{\theta}$ is learned either in a supervised setup [9]:

$$\arg \min_{\boldsymbol{\theta}} \mathbb{E}_{\mathbf{x}} \|\mathcal{E}(f_{\text{NM}}(\mathbf{x}, \boldsymbol{\theta})) - \mathbf{y}\|_2^2 + \lambda \mathbb{E}_{\mathbf{x}} \|f_{\text{NM}}(\mathbf{x}, \boldsymbol{\theta}) - \boldsymbol{\vartheta}\|_2^2 \quad (29)$$

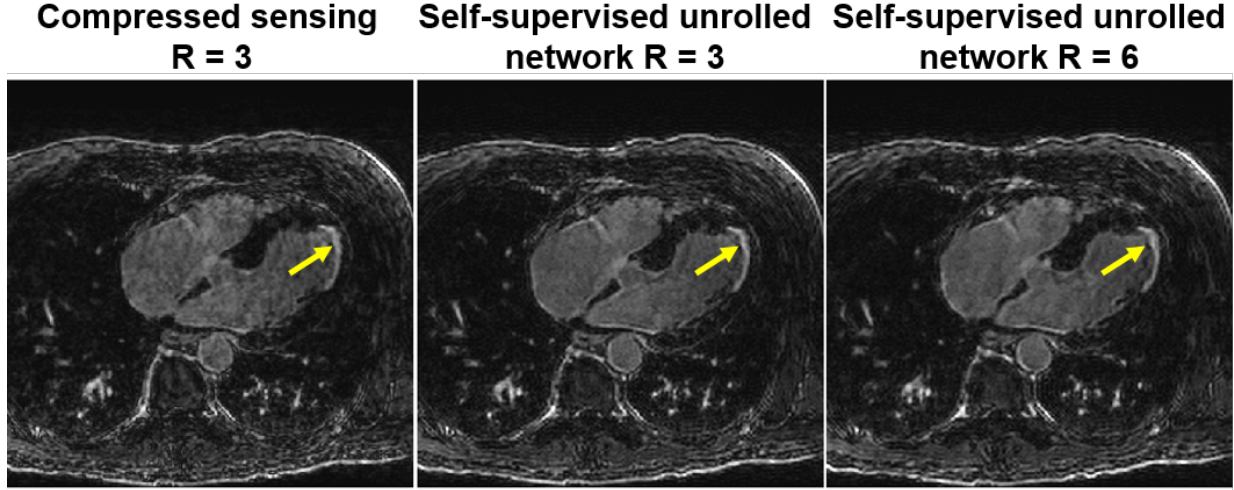


Fig. 6: Reconstruction results from a high-resolution late gadolinium enhancement acquisition on a cardiac patient (arrows: scar areas). This scan cannot be fully-sampled due to contrast-related scan time constraints. Unrolled networks can be trained in an unsupervised/self-supervised manner [59], leading to reconstructions that outperform current clinically used approaches, such as compressed sensing, and allowing acceleration rates twice as fast.

or in an unsupervised setup [60]

$$\arg \min_{\theta} \mathbb{E}_{\mathbf{x}} \|\mathcal{E}(f_{\text{NM}}(\mathbf{x}, \theta)) - \mathbf{y}\|_2^2 + \sum_i \lambda_i \mathcal{R}_i(f_{\text{NM}}(\mathbf{x}, \theta)), \quad (30)$$

where $\mathcal{R}_i(\cdot)$ are conventional regularizers that are not based on reference data, such as spatial total variation. In the following, we will expand on some applications for which non-linear forward models are beneficial.

1) Relaxivity mapping: MRI allows for quantitative measurements of inherent tissue parameters (T_1 , T_2 , T_2^* , $T_1\rho$), which is often referred to as relaxivity or quantitative mapping. In recent years, research developments have contributed towards the goal of retrieving multiple parametric maps from a single scan [4]. A model-based reconstruction in these cases eliminates the need for reconstructing individual images along the relaxivity curve, and the employed model acts as an intrinsic regularizer for the reconstruction. However, model-based reconstruction methods have prolonged reconstruction times compared to reconstruction of individual images followed by a parametric fitting, which hinders their clinical translation [4]. Deep learning models have been proposed to enable fast inference and shifting time-demanding workloads to the offline training procedure, showing feasibility in a number of quantitative mapping applications [9, 51]. In this setting, physics information has primarily been incorporated to the loss function during training, similar to Eqs. (29) and (30) [9, 60, 61]. Recently, networks that reflect low-rank subspace constraints have been proposed [62]. Generative models have also been studied to synthesize signal

evolutions suited for model-based reconstructions [63] or by extending the loss composition for more realistic estimations [64].

2) *Susceptibility mapping*: Physics-driven deep learning methods have also been studied in the context of quantitative susceptibility mapping. First works incorporated the physical principles of the dipole inversion model that describes the susceptibility-phase relationship into the loss function during neural network training [12]. Later works optimized the parameters in an unrolled gradient descent algorithm for nonlinear dipole inversion [65, 66]. More recently, the idea of fine-tuning pre-trained network weights on a scan-specific basis using the physics model was proposed [67], similar to the loss function in Eq. (30) without the additional regularizers.

3) *Flow, perfusion and contrast-enhanced MRI*: Flow imaging is used to measure blood velocities in the circulatory system, but requires considerable acquisition time. Thus, physics-driven deep learning methods have been proposed for improving flow imaging. These methods enforce fidelity to the physical model in the losses to a known ground-truth [68], or incorporate the physics of fluid flow by solving the partial differential equations via automatic differentiation in backpropagation [13]. Perfusion techniques provide ways to model blood flow often via the use of a kinetic model, but suffer from low-resolution or low signal-to-noise ratio acquisitions. Physics-driven methods incorporating the kinetic model to the loss function has been proposed [69]. In a similar vein, estimation of pharmacokinetic parameters from dynamic contrast-enhanced MRI by residual learning using the physical forward model [70] was also proposed for faster parameter inference.

4) *Motion*: Acquisitions under physiological and patient motion require methods for handling motion in order to avoid aliasing or blurring of the imaged anatomy. In addition to various prospective motion triggering, gating or correction methods, motion can be retrospectively modeled into the forward model and can thus be considered inside a motion-compensated/corrected reconstruction [5, 71]. These methods perform two fundamental operations: image registration and image reconstruction. Hence, they require reliable motion-resolved images from which the motion can be estimated. Motion field estimation can be controlled or supported by external motion surrogate signals [71] or initial motion field estimates [5].

While deep learning allows for efficient motion estimation, only few works embed motion estimation in image reconstruction. Among these, LAPNet formulates non-rigid registration directly in k-space [10, 72], inspired by the optical flow formulation. The estimated motion fields are then used to enhance the data consistency and exploit the information of all motion resolved states to reconstruct images of the body trunk. In the context of coronary MRI, a motion-informed MoDL network was proposed [11], using diffeomorphic motion fields estimated from the zero-filled images using a UNet and subsequent scaling and squaring layer. These motion fields are then embedded into the data consistency layer, solved via the

conjugate gradient algorithm as in MoDL. The network is unrolled for 3 iterations, with intermittent denoising networks. The full model is trained using a reconstruction loss and a motion estimation loss. For dynamic MR images, the whole temporal information was exploited by embedding motion-estimation UNets directly in the data consistency layers of an unrolled network architecture [73]. Hence, both reconstruction and motion estimation improve during as the motion-estimation networks rely on the reconstructions of the previous unrolled iteration. Further approaches achieved motion correction by rejecting motion-affected k-space lines [74] or subspace-constrained regularization [75]. Inspired by [76], a motion estimation network is embedded in a Batchelor-type reconstruction for Cartesian cine imaging [77]. An example reconstruction results of the systole and diastole for accelerations $R=4$ and $R=8$ is depicted in Figure 7.

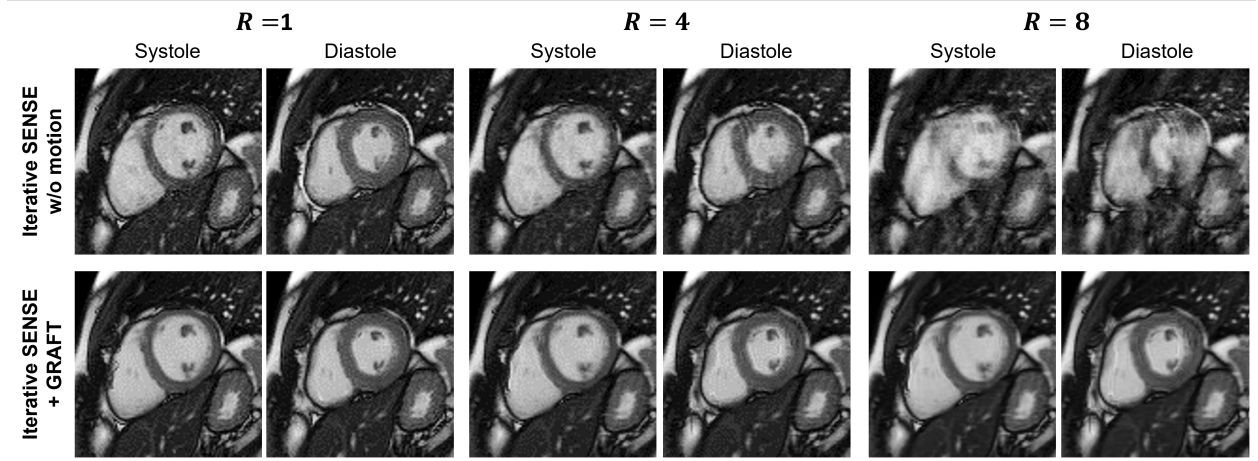


Fig. 7: Motion-Compensated reconstruction. A motion estimation network (GRAFT) is embedded in the reconstruction procedure [77]. The motion-compensated reconstruction outperforms iterative SENSE without motion compensation. If motion compensation is not performed, undersampling artifacts are substantially present. Systole and diastole frames are depicted for $R=1$, $R=4$ and $R=8$.

V. DISCUSSION

A. Issues and open problems

Deep learning has dominated research in computational MRI during the last few years, and while there are still a number of open questions and issues, both on the basic science and on the translational front, they evolved as the developments are going on in the field. During the early stages of the developments, access to raw MRI k-space training data was a major limiting factor that held the field back. The availability of open databases has largely removed this obstacle and public research challenges have also helped to

compare developed approaches on standardized datasets [54, 55]. However, they have also highlighted new issues. While it was demonstrated that deep learning models generally outperform handcrafted regularizers in iterative image reconstruction in terms of quantitative metrics like SSIM, PSNR and RMSE, their performance in the regime of over-regularization (when the influence of the prior becomes dominant because of the low-quality of the data) is challenging to assess. The results of classic regularizers like Tikhonov, total variation or ℓ_1 -wavelets in this scenario can be interpreted much easier by end-users. They lead to very characteristic artifact patterns that are easy to spot as being technical artifacts. Deep learning models have the computational capacity to generate realistic-looking images with either missing or artificially hallucinated image features [44] that are inconsistent with the measurement data if they are used at acceleration levels that are too high with respect to the encoding capabilities of the multi-element receive coil.

A solution is to move from qualitative image assessment towards the assessment of clinical outcomes. In particular, does the diagnostic quality improve for patients when deep learning methods are used instead of handcrafted regularizers? However, conducting such clinical studies is slow and costly, and in many cases an imaging exam cannot even be considered to be a true ground truth, which requires follow-ups with pathology or surgery departments.

Research challenges are also limited in terms of their ability to assess model generalization. The 2020 fastMRI challenge [55] included a track that specifically evaluated generalization with respect to deploying a trained model at a scanner from a different manufacturer. While the the winning models performed well in this test, the performance of some approaches was impacted negatively by trivial modifications in the data, for example whether raw data is saved with oversampling in the readout direction or not. In light of the substantial range of imaging parameters that can be changed during an MRI acquisition, it is still an open question if deep learning models should serve a general purpose role, or if specialized models should be tailored to a more narrow range of imaging settings for dedicated exams.

Another open issue of almost all developments is that they are performed retrospectively. While this is acceptable if true k-space raw data is used and no subtle data crime is performed [78], not all MR-signal-acquisition effects are captured with retrospective undersampling. In particular, effects related to spin-history, gradient and RF-hardware are usually not captured. This can cause issues when moving to prospective acquisitions on real MR-scanners. However, it should be pointed out that this is a general issue of all computational imaging methods that are developed retrospectively, and not a unique issue of deep learning techniques.

B. Domain-specific knowledge in post-processing and multi-task imaging

The medical imaging pipeline consists of many tasks that are mostly viewed separately. The imaging pipeline starts with data acquisition, followed by image reconstruction. The reconstructed image is then further analyzed using post-processing tasks, image segmentation, and quantitative evaluation, and/or methods for diagnosis and treatment planning are applied to facilitate medical decisions.

Thus, there have been efforts to combine several of these tasks into a multi-task imaging framework. Most work on solving multiple tasks jointly has been conducted in the field of motion-corrected image reconstruction, as summarized in Section IV-C4. In [74], joint motion detection, correction and segmentation was proposed. In contrast to the previously mentioned approaches, the motion was detected directly in k-space and, hence, influence the data consistency layer. Additionally, a bidirectional recurrent CNN (BCRNN) was used to account for spatio-temporal redundancies. The motion-corrected image was obtained by cascading 10 data consistency layers and BCRNNs. Afterwards, a UNet was applied for cardiac segmentation. Evaluated on the UK Biobank data, this work showed that training a joint network for reconstruction and segmentation outperforms sequential training of these networks.

A unified network for joint MRI reconstruction and segmentation was also proposed [79]. For image reconstruction, an unrolled network with alternating data consistency layers and denoising networks are used. The denoising networks are based on an encoder-decoder structure, where the encoder is shared with the image segmentation network. Hence, common features are extracted using the encoder, while the decoder adapts to the underlying task. Evaluation and simulation of k-space is performed on the MRBrainS segmentation challenge dataset. Their results suggests that high-quality segmentation benefits from this multi-task architecture. A similar conclusion was drawn using FR-Net [80], which consists of two submodules, a reconstruction network based on the fast iterative shrinkage-thresholding algorithm (FISTA), and a UNet for the segmentation of myocardium contours. The networks are trained using a combined reconstruction and segmentation loss, however, finding the right trade-off between these two terms is key for high-quality results. While these approaches both optimize for image reconstruction and another downstream task such as segmentation, it is still an open question if intermediately reconstructed images are needed, or if one could directly obtain, e.g., segmentation in k-space as proposed by [81].

Another interesting line of work incorporates domain knowledge into other post-processing tasks. In deformable image registration, data similarity was embedded in an unrolled gradient-descent network [82], similar to the ideas of Section III-D. This approach only requires the similarity measure to be differentiable. In medical image segmentation, there has been interest in incorporating prior domain knowledge about the shape, topology or location of the segmented object into the deep learning networks

to help with accuracy and improve weak/semi-supervision [83]. One common way to achieve this is to incorporate the prior domain knowledge into the training loss, similar to the ideas of Section III-A, including constraints on size, shape and topology of organs incorporated as regularization loss terms [83]. Another approach is analogous to the ideas of Section III-D applied to deformable models for segmentation, where the segmentation starts from a candidate shape that is topologically consistent, and the network learns the appropriate deformation to this shape to best match the labelled data [84].

VI. CONCLUSION

Physics-driven deep learning techniques are the current state-of-the-art methods for computational MRI. Spanning methods that incorporate physics of MRI acquisitions into loss functions to plug-and-play techniques, and generative models to unrolled networks, a large number of approaches have been proposed to improve the solution of linear and nonlinear inverse problems that arise in MRI. These methods are starting to make their way into translational and clinical settings, while also potentially altering the downstream tasks in the medical imaging pipeline. Thus, there are numerous opportunities for new technical developments and applications in physics-driven computational MRI from the signal processing community.

REFERENCES

- [1] Z.-P. Liang, F. E. Boada, et al., “Constrained reconstruction methods in MR imaging,” *Rev. Magn. Reson. Med.*, vol. 4, pp. 67–185, 1992.
- [2] K. P. Pruessmann, M. Weiger, M. B. Scheidegger, and P. Boesiger, “SENSE: Sensitivity encoding for fast MRI,” *Magn Reson Med*, vol. 42, no. 5, pp. 952–962, 1999.
- [3] M. Lustig, D. Donoho, and J. M. Pauly, “Sparse MRI: The application of compressed sensing for rapid MR imaging,” *Magn Reson Med*, vol. 58, no. 6, pp. 1182–1195, 2007.
- [4] N. Seiberlich, V. Gulani, et al., *Quantitative magnetic resonance imaging*, Academic Press, 2020.
- [5] P. Batchelor, D. Atkinson, et al., “Matrix description of general motion correction applied to multishot images,” *Magnetic Resonance in Medicine: An Official Journal of the International Society for Magnetic Resonance in Medicine*, vol. 54, no. 5, pp. 1273–1280, 2005.
- [6] K. Hammernik, T. Klatzer, et al., “Learning a variational network for reconstruction of accelerated MRI data,” *Mag Reson Med*, vol. 79, pp. 3055–71, 2018.
- [7] H. K. Aggarwal, M. P. Mani, and M. Jacob, “MoDL: Model-Based Deep Learning Architecture for Inverse Problems,” *IEEE Trans Med Imaging*, 2019.

- [8] F. Knoll, K. Hammernik, et al., “Deep-learning methods for parallel magnetic resonance imaging reconstruction,” *IEEE Signal Processing Magazine*, vol. 37, no. 1, pp. 128–140, 2020.
- [9] F. Liu, L. Feng, and R. Kijowski, “Mantis: Model-augmented neural network with incoherent k-space sampling for efficient mr parameter mapping,” *Magnetic resonance in medicine*, vol. 82, no. 1, pp. 174–188, 2019.
- [10] T. Küstner, J. Pan, et al., “Deep-learning based motion-corrected image reconstruction in 4D magnetic resonance imaging of the body trunk,” in *IEEE Asia-Pacific Signal and Information Processing Association (APSIPA)*, 2020.
- [11] H. Qi, R. Hajhosseiny, et al., “End-to-end deep learning nonrigid motion-corrected reconstruction for highly accelerated free-breathing coronary mra,” *Magnetic Resonance in Medicine*, vol. 86, no. 4, pp. 1983–1996, 2021.
- [12] J. Yoon, E. Gong, et al., “Quantitative susceptibility mapping using deep neural network: Qsmnet,” *Neuroimage*, vol. 179, pp. 199–206, 2018.
- [13] M. F. Fathi, I. Perez-Raya, et al., “Super-resolution and denoising of 4d-flow mri using physics-informed deep neural nets,” *Computer Methods and Programs in Biomedicine*, vol. 197, pp. 105729, 2020.
- [14] J. A. Fessler, “Optimization methods for magnetic resonance image reconstruction: Key models and optimization algorithms,” *IEEE Signal Processing Magazine*, vol. 37, no. 1, pp. 33–40, 2020.
- [15] J. Assländer, M. A. Cloos, et al., “Low rank alternating direction method of multipliers reconstruction for mr fingerprinting,” *Magnetic resonance in medicine*, vol. 79, no. 1, pp. 83–96, 2018.
- [16] D. Liang, J. Cheng, Z. Ke, and L. Ying, “Deep magnetic resonance image reconstruction: Inverse problems meet neural networks,” *IEEE Signal Process. Mag.*, vol. 37, no. 1, pp. 141–151, 2020.
- [17] S. Wang, Z. Su, et al., “Accelerating magnetic resonance imaging via deep learning,” in *IEEE International Symposium on Biomedical Imaging*, 2016, pp. 514–517.
- [18] C. M. Hyun, H. P. Kim, S. M. Lee, S. M. Lee, and J. K. Seo, “Deep learning for undersampled MRI reconstruction,” *Physics in Medicine and Biology*, vol. 63, no. 13, pp. 135007, 2018.
- [19] G. Yang, S. Yu, et al., “DAGAN: Deep De-Aliasing Generative Adversarial Networks for Fast Compressed Sensing MRI Reconstruction,” *IEEE Transactions on Medical Imaging*, vol. 37, no. 6, pp. 1310–1321, 2017.
- [20] M. Akcakaya, S. Moeller, S. Weingartner, and K. Ugurbil, “Scan-specific robust artificial-neural-networks for k-space interpolation (RAKI) reconstruction: Database-free deep learning for fast imaging,” *Magn Reson Med*, vol. 81, no. 1, pp. 439–453, Jan 2019.
- [21] R. Ahmad, C. A. Bouman, et al., “Plug-and-play methods for magnetic resonance imaging: Using

- denoisers for image recovery,” *IEEE Signal Processing Magazine*, vol. 37, no. 1, pp. 105–116, 2020.
- [22] J. Liu, Y. Sun, et al., “Rare: Image reconstruction using deep priors learned without groundtruth,” *IEEE Journal of Selected Topics in Signal Processing*, vol. 14, no. 6, pp. 1088–1099, 2020.
- [23] M. Mani, V. A. Magnotta, and M. Jacob, “qModel: A plug-and-play model-based reconstruction for highly accelerated multi-shot diffusion MRI using learned priors,” *Magn Reson Med*, vol. 86, no. 2, pp. 835–851, 08 2021.
- [24] J. Lehtinen, J. Munkberg, et al., “Noise2Noise: Learning image restoration without clean data,” in *Proceedings of the 35th International Conference on Machine Learning*. 2018, vol. 80, pp. 2965–2974, PMLR.
- [25] D. Ulyanov, A. Vedaldi, and V. Lempitsky, “Deep image prior,” *International Journal of Computer Vision*, vol. 128, no. 7, pp. 1867–1888, Mar. 2020.
- [26] A. P. Yazdanpanah, O. Afacan, and S. K. Warfield, “Non-learning based deep parallel MRI reconstruction (NLDpMRI),” in *Medical Imaging 2019: Image Processing*, E. D. Angelini and B. A. Landman, Eds. International Society for Optics and Photonics, 2019, vol. 10949, pp. 21 – 27, SPIE.
- [27] J. Yoo, K. H. Jin, et al., “Time-dependent deep image prior for dynamic mri,” *IEEE Transactions on Medical Imaging*, vol. 40, no. 12, pp. 3337–3348, 2021.
- [28] D. Zhao, Y. Huang, F. Zhao, B. Qin, and J. Zheng, “Reference-driven undersampled MR image reconstruction using wavelet sparsity-constrained deep image prior,” *Comput. Math. Methods Medicine*, vol. 2021, pp. 8865582:1–8865582:12, 2021.
- [29] M. Mardani, E. Gong, et al., “Deep Generative Adversarial Neural Networks for Compressive Sensing (GANCS) MRI,” *IEEE Transactions on Medical Imaging*, vol. PP, no. c, pp. 1, 2018.
- [30] V. Edupuganti, M. Mardani, S. Vasanawala, and J. Pauly, “Uncertainty quantification in deep mri reconstruction,” *IEEE Transactions on Medical Imaging*, vol. 40, no. 1, pp. 239–250, 2021.
- [31] D. Narnhofer, K. Hammernik, F. Knoll, and T. Pock, “Inverse GANs for accelerated MRI reconstruction,” in *Wavelets and Sparsity XVIII*, D. V. D. Ville, M. Papadakis, and Y. M. Lu, Eds. International Society for Optics and Photonics, 2019, vol. 11138, pp. 381 – 392, SPIE.
- [32] G. Oh, B. Sim, H. Chung, L. Sunwoo, and J. C. Ye, “Unpaired deep learning for accelerated mri using optimal transport driven cyclegan,” *IEEE Transactions on Computational Imaging*, vol. 6, pp. 1285–1296, 2020.
- [33] K. Gregor and Y. LeCun, “Learning fast approximations of sparse coding,” in *Proc. 27th International Conference on International Conference on Machine Learning*, USA, 2010, ICML’10,

- pp. 399–406, Omnipress.
- [34] Y. Yang, J. Sun, H. Li, and Z. Xu, “Deep ADMM-Net for Compressive Sensing MRI,” in *Advances in Neural Information Processing Systems (NIPS)*, 2016, number Nips, pp. 10–18.
 - [35] J. Schlemper, J. Caballero, J. V. Hajnal, A. N. Price, and D. Rueckert, “A deep cascade of convolutional neural networks for dynamic MR image reconstruction,” *IEEE Trans Med Imaging*, vol. 37, no. 2, pp. 491–503, 2018.
 - [36] C. Qin, J. Schlemper, et al., “Convolutional recurrent neural networks for dynamic MR image reconstruction,” *IEEE Transactions on Medical Imaging*, 2019.
 - [37] J. Cheng, H. Wang, L. Ying, and D. Liang, “Model learning: Primal dual networks for fast MR imaging,” in *Medical Image Computing and Computer Assisted Intervention - MICCAI 2019 - 22nd International Conference, Shenzhen, China, October 13-17, 2019, Proceedings, Part III*, D. Shen, T. Liu, et al., Eds. 2019, vol. 11766 of *Lecture Notes in Computer Science*, pp. 21–29, Springer.
 - [38] J. Duan, J. Schlemper, et al., “Vs-net: Variable splitting network for accelerated parallel MRI reconstruction,” in *Lecture Notes in Computer Science (including subseries Lecture Notes in Artificial Intelligence and Lecture Notes in Bioinformatics)*, 2019, vol. 11767 LNCS, pp. 713–722.
 - [39] B. Yaman, S. A. H. Hosseini, et al., “Self-Supervised Learning of Physics-Guided Reconstruction Neural Networks without Fully-Sampled Reference Data,” *Magn Reson Med*, vol. 84, no. 6, pp. 3172–3191, Dec 2020.
 - [40] S. A. H. Hosseini, B. Yaman, S. Moeller, M. Hong, and M. Akçakaya, “Dense recurrent neural networks for accelerated MRI: history-cognizant unrolling of optimization algorithms,” *IEEE J. Sel. Top. Signal Process.*, vol. 14, no. 6, pp. 1280–1291, 2020.
 - [41] S. Roth and M. J. Black, “Fields of Experts,” *International Journal of Computer Vision*, vol. 82, no. 2, pp. 205–229, 2009.
 - [42] D. Narnhofer, A. Effland, et al., “Bayesian uncertainty estimation of learned variational mri reconstruction,” *IEEE Transactions on Medical Imaging*, vol. 41, no. 2, pp. 279–291, 2022.
 - [43] A. Sriram, J. Zbontar, et al., “End-to-end variational networks for accelerated mri reconstruction,” 2020.
 - [44] K. Hammernik, J. Schlemper, et al., “Systematic evaluation of iterative deep neural networks for fast parallel mri reconstruction with sensitivity-weighted coil combination,” *Magnetic Resonance in Medicine*, vol. 86, no. 4, pp. 1859–1872, 2021.
 - [45] M. Mardani, Q. Sun, et al., “Neural proximal gradient descent for compressive imaging,” in *Proceedings of the 32nd International Conference on Neural Information Processing Systems*, Red Hook, NY, USA, 2018, NIPS’18, p. 9596–9606, Curran Associates Inc.

- [46] M. Akçakaya, B. Yaman, H. Chung, and J. C. Ye, “Unsupervised deep learning methods for biological image reconstruction and enhancement,” *IEEE Signal Process. Mag.*, March 2022.
- [47] H. K. Aggarwal, A. Pramanik, and M. Jacob, “Ensure: Ensemble stein’s unbiased risk estimator for unsupervised learning,” in *ICASSP*. 2021, pp. 1160–1164, IEEE.
- [48] B. Yaman, S. A. H. Hosseini, and M. Akcakaya, “Zero-shot self-supervised learning for MRI reconstruction,” in *International Conference on Learning Representations*, 2022.
- [49] M. Kellman, K. Zhang, et al., “Memory-efficient learning for large-scale computational imaging,” *IEEE Trans Comp Imaging*, vol. 6, pp. 1403–1414, 2020.
- [50] D. Gilton, G. Ongie, and R. Willett, “Deep equilibrium architectures for inverse problems in imaging,” *IEEE Transactions on Computational Imaging*, vol. 7, pp. 1123–1133, 2021.
- [51] P. Virtue, S. X. Yu, and M. Lustig, “Better than real: Complex-valued neural nets for MRI fingerprinting,” *IEEE International Conference on Image Processing*, vol. 2017-Septe, pp. 3953–3957, 2018.
- [52] C. Trabelsi, O. Bilaniuk, et al., “Deep complex networks,” *arXiv preprint arXiv:1705.09792*, 2017.
- [53] Y. Wang, Y. Song, et al., “Reduction of Gibbs artifacts in magnetic resonance imaging based on Convolutional Neural Network,” *Proceedings - 2017 10th International Congress on Image and Signal Processing, BioMedical Engineering and Informatics, CISP-BMEI 2017*, vol. 2018-Janua, no. 2, 2018.
- [54] F. Knoll, T. Murrell, et al., “Advancing machine learning for mr image reconstruction with an open competition: Overview of the 2019 fastmri challenge,” *Magnetic Resonance in Medicine*, vol. 84, pp. 2054–3070, 6 2020.
- [55] M. J. Muckley, B. Riemenschneider, et al., “Results of the 2020 fastmri challenge for machine learning MR image reconstruction,” *IEEE Trans. Medical Imaging*, vol. 40, no. 9, pp. 2306–2317, 2021.
- [56] P. M. Johnson, G. Jeong, et al., “Evaluation of the robustness of learned MR image reconstruction to systematic deviations between training and test data for the models from the fastMRI challenge,” in *Machine Learning for Medical Image Reconstruction*, pp. 25–34. 2021.
- [57] T. Küstner, N. Fuin, et al., “CINENet: deep learning-based 3D cardiac CINE MRI reconstruction with multi-coil complex-valued 4D spatio-temporal convolutions,” *Sci Rep*, vol. 10, no. 13710, 2020.
- [58] Z. Huang, J. Bae, et al., “A Simulation Pipeline to Generate Realistic Breast Images for Learning DCE-MRI Reconstruction,” *Machine Learning for Medical Image Reconstruction*, vol. 12964, 2021.
- [59] B. Yaman, C. Shenoy, et al., “Self-supervised physics-guided deep learning reconstruction for high-

- resolution 3d lge cmr,” in *2021 IEEE 18th International Symposium on Biomedical Imaging (ISBI)*, 2021, pp. 100–104.
- [60] F. Liu, R. Kijowski, G. El Fakhri, and L. Feng, “Magnetic resonance parameter mapping using model-guided self-supervised deep learning,” *Magnetic Resonance in Medicine*, vol. 85, no. 6, pp. 3211–3226, 2021.
- [61] M. Torop, S. V. V. N. Kothapalli, et al., “Deep learning using a biophysical model for robust and accelerated reconstruction of quantitative, artifact-free and denoised images,” *Magnetic Resonance in Medicine*, vol. 84, no. 6, pp. 2932–2942, 2020.
- [62] Y. Li, Y. Wang, et al., “Deep learning-enhanced t1 mapping with spatial-temporal and physical constraint,” *Magnetic Resonance in Medicine*, vol. 86, no. 3, pp. 1647–1661, 2021.
- [63] M. Yang, Y. Jiang, D. Ma, B. B. Mehta, and M. A. Griswold, “Game of learning bloch equation simulations for mr fingerprinting,” *arXiv preprint arXiv:2004.02270*, 2020.
- [64] F. Liu, R. Kijowski, L. Feng, and G. El Fakhri, “High-performance rapid mr parameter mapping using model-based deep adversarial learning,” *Magnetic Resonance Imaging*, vol. 74, pp. 152–160, 2020.
- [65] D. Polak, I. Chatnuntawech, et al., “Nonlinear dipole inversion (ndi) enables quantitative susceptibility mapping (qsm) without parameter tuning,” *arXiv preprint arXiv:1909.13692*, 2019.
- [66] R. Feng, J. Zhao, et al., “Modl-qsm: Model-based deep learning for quantitative susceptibility mapping,” *NeuroImage*, vol. 240, pp. 118376, 2021.
- [67] J. Zhang, Z. Liu, et al., “Fidelity imposed network edit (fine) for solving ill-posed image reconstruction,” *NeuroImage*, vol. 211, pp. 116579, 2020.
- [68] E. Ferdian, A. Suinesiaputra, et al., “4DFlowNet: super-resolution 4D flow MRI using deep learning and computational fluid dynamics,” *Frontiers in Physics*, vol. 8, pp. 138, 2020.
- [69] C. Ulas, G. Tetteh, S. Kaczmarz, C. Preibisch, and B. H. Menze, “Deepasl: Kinetic model incorporated loss for denoising arterial spin labeled mri via deep residual learning,” in *International conference on medical image computing and computer-assisted intervention*. Springer, 2018, pp. 30–38.
- [70] C. Ulas, G. Tetteh, et al., “Direct estimation of pharmacokinetic parameters from dce-mri using deep cnn with forward physical model loss,” in *International Conference on Medical Image Computing and Computer-Assisted Intervention*. Springer, 2018, pp. 39–47.
- [71] F. Odille, N. Cindea, et al., “Generalized MRI reconstruction including elastic physiological motion and coil sensitivity encoding,” *Magn Reson Med*, vol. 59, no. 6, pp. 1401–1411, jun 2008.
- [72] T. Küstner, J. Pan, et al., “Lapnet: Non-rigid registration derived in k-space for magnetic resonance

- imaging,” *IEEE Transactions on Medical Imaging*, vol. 40, no. 12, pp. 3686–3697, 2021.
- [73] G. Seegoolam, J. Schlemper, et al., “Exploiting motion for deep learning reconstruction of extremely-undersampled dynamic mri,” in *Medical Image Computing and Computer Assisted Intervention – MICCAI 2019*, D. Shen, T. Liu, et al., Eds., Cham, 2019, pp. 704–712, Springer International Publishing.
- [74] I. Oksuz, J. R. Clough, et al., “Deep learning-based detection and correction of cardiac mr motion artefacts during reconstruction for high-quality segmentation,” *IEEE Transactions on Medical Imaging*, vol. 39, pp. 4001–4010, 12 2020.
- [75] S. Biswas, H. K. Aggarwal, and M. Jacob, “Dynamic mri using model-based deep learning and storm priors: Modl-storm,” *Magnetic resonance in medicine*, vol. 82, no. 1, pp. 485–494, 2019.
- [76] G. Cruz, K. Hammernik, T. Kuestner, and et al., “One-heartbeat cardiac cine imaging via jointly regularized non-rigid motion corrected reconstruction,” in *Proc. International Society for Magnetic Resonance in Medicine (ISMRM)*, 2021, p. 0070.
- [77] K. Hammernik, J. Pan, D. Rueckert, and T. Küstner, “Motion-guided physics-based learning for cardiac mri reconstruction,” in *2021 55th Asilomar Conference on Signals, Systems, and Computers*, 2021, pp. 900–907.
- [78] E. Shimron, J. I. Tamir, K. Wang, and M. Lustig, “Subtle inverse crimes: Naïvely training machine learning algorithms could lead to overly-optimistic results,” *CoRR*, vol. abs/2109.08237, 2021.
- [79] L. Sun, Z. Fan, X. Ding, Y. Huang, and J. Paisley, “Joint cs-mri reconstruction and segmentation with a unified deep network,” *Lecture Notes in Computer Science (including subseries Lecture Notes in Artificial Intelligence and Lecture Notes in Bioinformatics)*, vol. 11492 LNCS, pp. 492–504, 6 2019.
- [80] Q. Huang, D. Yang, J. Yi, L. Axel, and D. Metaxas, “Fr-net: Joint reconstruction and segmentation in compressed sensing cardiac mri,” *Lecture Notes in Computer Science (including subseries Lecture Notes in Artificial Intelligence and Lecture Notes in Bioinformatics)*, vol. 11504 LNCS, pp. 352–360, 6 2019.
- [81] J. Schlemper, O. Oktay, et al., “Cardiac mr segmentation from undersampled k-space using deep latent representation learning,” *Lecture Notes in Computer Science (including subseries Lecture Notes in Artificial Intelligence and Lecture Notes in Bioinformatics)*, vol. 11070 LNCS, pp. 259–267, 9 2018.
- [82] H. Qiu, K. Hammernik, C. Qin, and D. Rueckert, “Gradirn: Learning iterative gradient descent-based energy minimization for deformable image registration,” *CoRR*, vol. abs/2112.03915, 2021.
- [83] R. El Jurdi, C. Petitjean, P. Honeine, V. Cheplygina, and F. Abdallah, “High-level prior-based loss

- functions for medical image segmentation: A survey,” *Computer Vision and Image Understanding*, vol. 210, pp. 103248, 2021.
- [84] J. R. Clough, N. Byrne, et al., “A topological loss function for deep-learning based image segmentation using persistent homology,” *arXiv preprint arXiv:1910.01877*, 2019.